Numerical simulations of diffusive shock acceleration in SNRs

V.N.Zirakashvili, V.S.Ptuskin

Pushkov Institute for Terrestrial Magnetism, Ionosphere and Radiowave Propagation, 142190, Troitsk, Moscow Region, Russia

Abstract

A new numerical model of the nonlinear diffusive shock acceleration is presented. It is used for modeling of particle acceleration in supernova remnants. The model contains coupled spherically symmetric hydrodynamic equations and the transport equations for energetic protons, ions and electrons. The forward and reverse shocks are included in the consideration. The spectra of cosmic rays released into interstellar medium from a supernova remnant are determined. The role of the reverse shock in the production of CR ions and positrons is discussed.

Keywords:
cosmic rays, acceleration, supernova remnants

1. Introduction

The diffusive shock acceleration (DSA) process [1, 2, 3, 4] is considered as the principal mechanism for production of galactic cosmic rays (CR) in supernova remnants (SNRs). A significant theoretical progress in the investigation of this mechanism was achieved (see e.g. Malkov & Drury [5] for a review). However only during the last decade the excellent results of X-ray and gamma-ray astronomy supplied the observational evidence of the presence of multi-TeV energetic particles in these objects (see e.g. Aharonian et al. [6]).

Two shocks are produced by super-sonically moving supernova ejecta after an explosion. A forward shock propagates in the circumstellar medium while a reverse shock propagates in the gas of ejecta. Generally it is believed that some part of thermal particles is injected at the shock fronts into acceleration.

In this paper we present a new numerical model of nonlinear diffusive shock acceleration. This model is a natural development of the existing models [7, 8]. The solution of spherically symmetric hydrodynamic equations is combined with the energetic particle transport and acceleration at the forward and reverse shocks of a supernova remnant. Nonlinear response of energetic particles via their pressure gradient results in the self-regulation of acceleration efficiency.

Our previous studies that used this model dealt with the CR spectra produced by SNRs [9, 10]. The input of the reverse shock was not taken into account there while the acceleration by both shocks was considered for modeling of non-thermal electromagnetic emission from the SNR RX J1713.7-3946 [11].

The paper is organized as follows. The short description of the model is given in Sect. 2. The results of modeling of evolution of a supernova remnant in the interstellar medium are presented in Sect. 3. Sect. 4 contains the discussion of our results. Our conclusions are given in the last Section. The numerical code is described in Appendix.

2. Nonlinear model of diffusive shock acceleration

Hydrodynamical equations for the gas density $\rho(r, t)$, gas velocity $u(r, t)$, gas pressure $P_g(r, t)$, and the equation for isotropic part of the CR proton momentum distribution $N(r, t, p)$ in the spherically symmetrical case are given by

$$\frac{\partial \rho}{\partial t} = -\frac{1}{r^2}\frac{\partial}{\partial r}r^2 u\rho \qquad (1)$$

$$\frac{\partial u}{\partial t} = -u\frac{\partial u}{\partial r} - \frac{1}{\rho}\left(\frac{\partial P_g}{\partial r} + \frac{\partial P_c}{\partial r}\right) \qquad (2)$$

$$\frac{\partial P_g}{\partial t} = -u\frac{\partial P_g}{\partial r} - \frac{\gamma_g P_g}{r^2}\frac{\partial r^2 u}{\partial r} - (\gamma_g - 1)(w - u)\frac{\partial P_c}{\partial r} \qquad (3)$$

$$\frac{\partial N}{\partial t} = \frac{1}{r^2}\frac{\partial}{\partial r}r^2 D(p, r, t)\frac{\partial N}{\partial r} - w\frac{\partial N}{\partial r} + \frac{\partial N}{\partial p}\frac{p}{3r^2}\frac{\partial r^2 w}{\partial r}$$

$$+ \frac{\eta^f \delta(p - p_f)}{4\pi p_f^2 m}\rho(R_f + 0, t)(\dot{R}_f - u(R_f + 0, t))\delta(r - R_f(t))$$

$$+ \frac{\eta^b \delta(p - p_b)}{4\pi p_b^2 m}\rho(R_b - 0, t)(u(R_b - 0, t) - \dot{R}_b)\delta(r - R_b(t)) \quad (4)$$

Here $P_c = 4\pi \int p^2 dp v p N/3$ is the CR pressure, $w(r, t)$ is the advective velocity of CRs, γ_g is the adiabatic index of the gas, and $D(r, t, p)$ is the CR diffusion coefficient. It was assumed that the diffusive streaming of CRs results in the generation of magnetohydrodynamic (MHD) waves. CR particles are scattered by these waves. That is why the CR advective velocity w may differ from the gas velocity u. Damping of these waves results in an additional gas heating. It is described by the last term in Eq. (3). Two last terms in Eq. (4) correspond to the injection of thermal protons with momenta $p = p_f$, $p = p_b$ and mass m at the fronts of the forward and reverse shocks at $r = R_f(t)$ and

$r = R_b(t)$ respectively[1]. The dimensionless parameters η^f and η^b determine the injection efficiency.

The equation for ions is similar to Eq. (4). For ions with the mass $M = Am$ and the mass number A it is convenient to use the momentum per nucleon p and the normalization of the ion spectra N_i to the baryonic number density. Then the number density of ions n_i is $n_i = 4\pi A^{-1} \int p^2 dp N_i$. The ion pressure $P_i = 4\pi \int p^2 dp v p N_i/3$ is also taken into account in the cosmic ray pressure P_c.

We shall neglect the pressure of energetic electrons. In other words they are treated as the test particles. The evolution of electron distribution is described by equation similar to Eq. (4) with additional terms describing synchrotron and inverse Compton (IC) losses.

CR diffusion is determined by magnetic inhomogeneities. Strong streaming of accelerated particles changes medium properties in the shock vicinity. CR streaming instability results in the high level of MHD turbulence [2] and even in the amplification of magnetic field in young SNRs [12]. Due to this effect the maximum energy of accelerated particles may be higher in comparison with previous estimates of Lagage and Cesarsky [14].

According to the numerical modeling of this non-resonant instability, the magnetic field is amplified by the flux of run-away highest energy particles in the relatively broad region upstream of the shock [13]. Magnetic energy density is a small fraction ($\sim 10^{-3}$) of the energy density of accelerated particles. This amplified almost isotropic magnetic field can be considered as a large-scale magnetic field for lower energy particles which are concentrated in the narrow region upstream of the shock. Resonant streaming instability of these particles produces MHD waves propagating in the direction opposite to the CR gradient. Strong nonlinear damping of these waves results in the gas heating (see the last term in Eq.(3)). CR gradient is negative upstream of the forward shock and MHD waves propagate in the positive direction. The situation changes downstream of the forward shock where CR gradient is as a rule positive and MHD waves propagate in the negative direction. This effect is mostly pronounced downstream of the forward shock of SNR because the magnetic field is additionally amplified by the shock compression and the Alfvén velocity $V_A = B/\sqrt{4\pi\rho}$ can be comparable with the gas velocity in the shock frame $u' = \dot{R}_f - u(R_f - 0, t)$. As for CR diffusion coefficient, it is probably close to the Bohm value $D_B = pvc/3qB$, where q is the electric charge of particles.

We apply a finite-difference method to solve Eqs (1-4) numerically upstream and downstream of the forward and reverse shock (see Appendix). A non-uniform numerical grid upstream of the shocks at $r > R_f$ and $r < R_b$ allows to resolve small scales of hydrodynamical quantities appearing due to the pressure gradient of low-energy CRs. The gases compressed at the forward and reverse shocks are separated by a contact discontinuity at $r = R_c$ that is situated between the shocks. An explicit

conservative TVD scheme [15] for hydrodynamical equations (1-3) and uniform spatial grid were used between the shocks.

Because of synchrotron losses the spacial scale of the high-energy electrons can be rather small downstream of the shocks. That is why we use a non-uniform numerical spacial grid for accelerated electrons downstream of the shocks.

The magnetic field plays no dynamical role in the model. Since we have not perform the modeling of the amplification and transport of magnetic field here, its coordinate dependence should be specified for determination of cosmic ray diffusion and for calculation of synchrotron emission and losses. We shall assume below that the coordinate dependencies of the magnetic field and the gas density coincide upstream and downstream of the forward shock:

$$B(r,t) = B_0 \frac{\rho}{\rho_0} \sqrt{\frac{\dot{R}_f^2}{M_A^2 V_{A0}^2} + 1}, \ r > R_c. \tag{5}$$

Here ρ_0 is the gas density and $V_{A0} = B_0/\sqrt{4\pi\rho_0}$ is the Alfvén velocity of the circumstellar medium. The parameter M_A determines the value of the amplified magnetic field strength. For low shock velocities $\dot{R}_f < M_A V_{A0}$ the magnetic field is not amplified.

The magnetic energy is about 3.5 percent of the dynamical pressure $\rho_0 \dot{R}^2$ according to estimates from the width of X-ray filaments in young SNRs [16]. This number and characteristic compression ratio of a modified SNR shock $\sigma = 6$ correspond to $M_A \approx 23$. Since the plasma density ρ decreases towards the contact discontinuity downstream of the forward shock, the same is true for the magnetic field strength according to Eq. (5). This seems reasonable because of a possible magnetic dissipation in this region.

Situation is different downstream of the reverse shock at $R_b < r < R_c$. The plasma flow is as a rule strongly influenced by the Rayleigh-Taylor instability that occurs in the vicinity of the contact discontinuity and results in the generation of MHD turbulence in this region. We shall assume that the magnetic field does not depend on radius downstream of the reverse shock while the dependence in the upstream region is described by the equation similar to Eq. (5):

$$B(r,t) = \sqrt{4\pi\rho_m} \frac{|\dot{R}_b - u(r_m)|}{M_A} \begin{cases} 1, \ r < r_m, \\ \rho/\rho_m, \\ r_m < r < R_b, \\ \rho(R_b + 0)/\rho_m, \\ R_b < r < R_c \end{cases} \tag{6}$$

Here $r_m < R_b$ is the radius where the ejecta density has a minimum and equals ρ_m. This radius r_m is generally close to the reverse shock radius R_b and is equal to it if the reverse shock is not modified by the cosmic ray pressure.

CR advective velocity may differ from the gas velocity on the value of the radial component of the Alfvén velocity V_{Ar} calculated in the isotropic random magnetic field: $w = u + \xi_A V_A/\sqrt{3}$. Here the factor ξ_A describes the possible deviation of the cosmic ray drift velocity from the gas velocity. The similar expression for the cosmic ray drift velocity is used upstream of

---

[1] We shall use indexes f and b for quantities corresponding to the forward and reverse (backward) shock respectively.
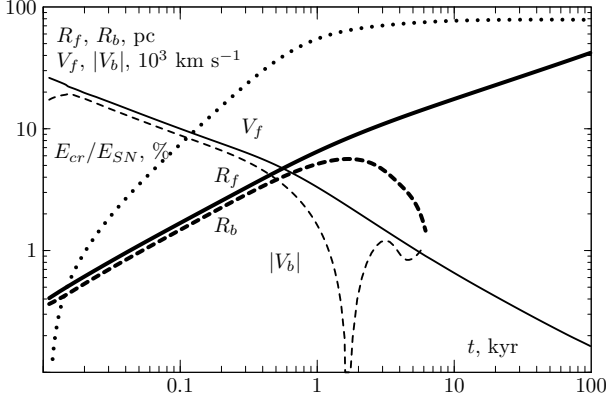
Figure 1: Dependencies on time of the forward shock radius R_f (thick solid line), the reverse shock radius R_b (thick dashed line), the forward shock velocity V_f (thin solid line) and the reverse shock velocity V_b (thin dashed line). The ratio of CR energy and energy of supernova explosion E_{cr}/E_{SN} (dotted line) is also shown.
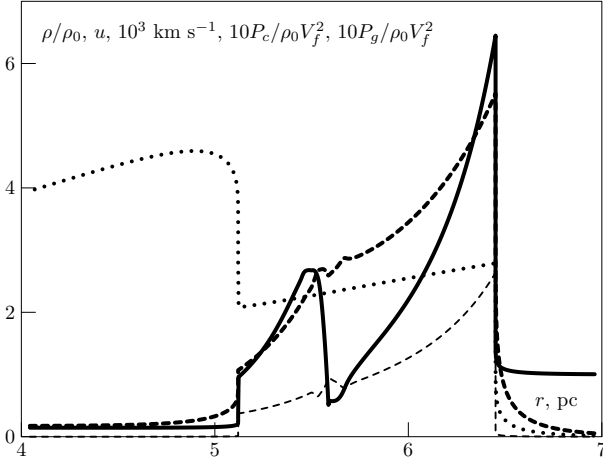

Figure 2: Radial dependencies of the gas density (thick solid line), the gas velocity (dotted line), CR pressure (thick dashed line) and the gas pressure (dashed line) at $t = 10^3$ yr. At this epoch the forward shock velocity is 3300 km s^{-1}, its radius is 6.5 pc, the reverse shock velocity is 1650 km s^{-1}, its radius is 5.1 pc, the magnetic field strength downstream of the forward shock is 160 μG while the magnetic field strength downstream the reverse shock is 56 μG.

the reverse shock at $r < R_b$. We shall use values $\xi_A = 1$ and $\xi_A = -1$ upstream of the forward and reverse shocks respectively, where Alfvén waves are generated by the cosmic ray streaming instability and propagate in the corresponding directions. The damping of these waves heats the gas upstream of the shocks [17] and limits the total compression ratios by a number close to 6. This Alfvén heating produce a more efficient limitation of the shock modification in comparison with the dynamical effects of the magnetic field considered by Caprioli et al. [18] which are neglected in our study. In the downstream region of the forward and reverse shock at $R_b < r < R_f$ we set $\xi_A = 0$ and therefore $w = u$ in the major part of this paper except the consideration of the Alfvén drift effects downstream of the shocks at the end of Sect.3 and in Fig.10.

We shall use the following diffusion coefficient

$$D = \eta_B D_B \begin{cases} \left(1 + \frac{M_A^2 V_{A0}^2}{\dot{R}_f^2}\right)^g \exp\left(\frac{r - R_f}{\xi_0 R_f}\right), & r > R_f, \\ \left(1 + \frac{M_A^2 V_{A0}^2}{\dot{R}_f^2}\right)^g, & R_c < r < R_f, \\ 1, & R_b < r < R_c, \\ \exp\left(\frac{R_b - r}{\xi_0 R_b}\right), & r < R_b. \end{cases} \quad (7)$$

Here the parameter $g > 0$ depends on the type of nonlinear wave damping which is relevant only for low velocity shocks $\dot{R}_f < M_A V_{A0}$ when the magnetic field is not amplified. The parameter η_B describes the possible deviations of diffusion coefficient from the Bohm value $D_B = vpc/3qB(r, t)$ for high-velocity shocks. Since the highest energy particles are scattered by small-scale magnetic fields, their diffusion is faster than the Bohm diffusion [13]. The same is true for smaller energy particles because they can be resonantly scattered only by a fraction of the magnetic spectrum. We shall use the value $\eta_B = 2$ throughout the paper.

We shall use the value of parameter $g = 1.5$ below. It corresponds to the nonlinear wave damping of the weak turbulence theory. Note that a stronger Kolmogorov-type nonlinear damping used by Ptuskin & Zirakashvili [19] for estimate of maximum energy in SNRs corresponds to $g = 3$.

In real situation the level of MHD turbulence drops with distance upstream of the shock and diffusion may be even faster there. This is qualitatively taken into account by the exponential factors in Eq. (7). The characteristic diffusive scale of highest energy particles is a small fraction $\xi_0 \ll 1$ of the shock radius [13] and is determined by the generation and transport of MHD turbulence in the upstream region [20, 21]. The value $\xi_0 \sim \ln^{-1}(D_c/D_s)$ is determined by ratio of diffusion coefficient D_c in the circumstellar medium and diffusion coefficient $D_s \ll D_c$ in the vicinity of the shock. The MHD turbulence is amplified exponentially in time before the shock arrival from the background level by cosmic ray streaming instability. The characteristic range of ξ_0 is $0.05 \div 0.1$ [13]. We shall use the value $\xi_0 = 0.05$ below.

It is believed that the supernova ejecta has some velocity distribution $P(V)$ just after the supernova explosion [22]

$$P(V) = \frac{3(k - 3)}{4\pi k} \begin{cases} 1, & V < V_{ej} \\ \left(V/V_{ej}\right)^{-k}, & V > V_{ej}. \end{cases} \quad (8)$$

Here the index k characterizes the steep power-low part of this distribution. The radial distribution of ejecta density is described by the same expression with $V = r/t$. The characteristic ejecta velocity V_{ej} can be expressed in terms of energy of supernova explosion E_{SN} and ejecta mass M_{ej} as

$$V_{ej} = \left(\frac{10(k - 5)E_{SN}}{3(k - 3)M_{ej}}\right)^{1/2}. \quad (9)$$

3. Numerical results

Figures (1)-(9) illustrate the numerical results that are obtained for the SNR shock propagating in the medium with
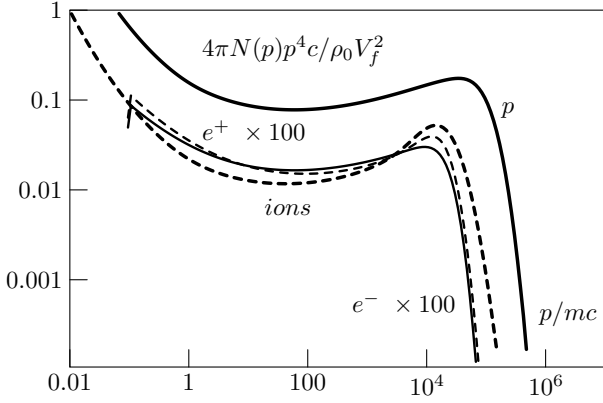
3

Figure 3: Spectra of accelerated particles at $t = 10^3$ yr. The proton spectrum at the forward shock (thick solid), ion spectrum at the reverse shock (thick dashed), electron spectrum at the forward shock (multiplied to the factor of 100, thin solid) and positron spectrum at the reverse shock (multiplied to the factor of 100, thin dashed) are shown. Spectrum of ions is shown as the function of momentum per nucleon and normalized to the baryonic number density.

Figure 5: Spectra of accelerated particles at $t = 10^4$ yr. The spectrum of protons (thick solid line) and electrons (multiplied to the factor of 100, thin solid line) at the forward shock, ion spectrum (thick dashed line) and positron spectrum (multiplied to the factor of 100, thin dashed line) in the central part of the remnant are shown. Spectrum of ions is shown as the function of momentum per nucleon and normalized to baryonic number density.
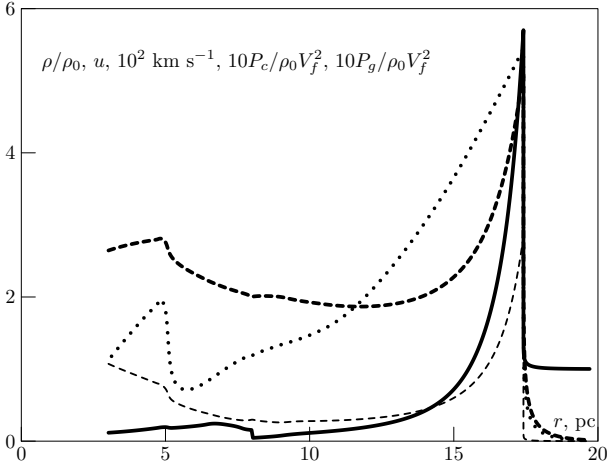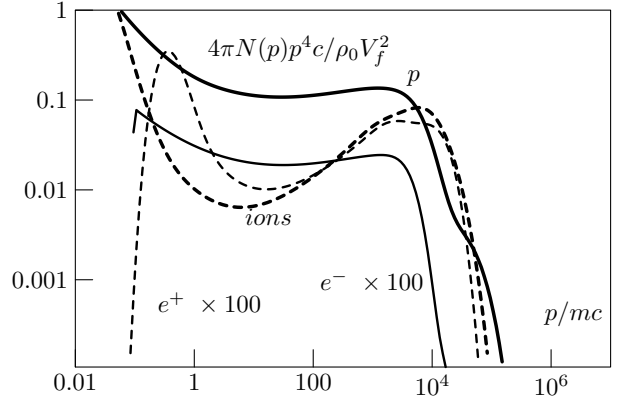

Figure 4: Radial dependencies of the gas density (thick solid line), the gas velocity (dotted line), CR pressure (thick dashed line) and the gas pressure (dashed line) at $t = 10^4$ yr. At this epoch the forward shock velocity is 660 km s^{-1}, its radius is 17 pc, magnetic field strength downstream of the forward shock is 40 μG.

a hydrogen number density $n_H = 0.1$ cm^{-3}, magnetic field strength $B_0 = 5$ μG and temperature $T = 10^4$ K. The fraction $x_{He} = n_{He}/n_H = 0.1$ of helium nuclei was assumed. The gas of ejecta does not contain hydrogen in the case considered. We use the ejecta mass $M_{ej} = 1.4 M_\odot$, the energy of explosion $E_{SN} = 1.0 \cdot 10^{51}$ erg and the parameter of ejecta velocity distribution $k = 7$. The value of the parameter $M_A = 23$ was assumed.

The initial forward shock velocity is $V_0 = 2.9 \cdot 10^4$ km s^{-1}. The injection efficiency is taken to be independent on time $\eta^b = \eta^f = 0.01$, and the injection momenta are $p_f = 2m(\dot{R}_f - u(R + 0, t))$, $p_b = 2m(u(R_b - 0, t) - \dot{R}_b)$. Protons with a mass m are injected at the forward shock while ions with mass number A and charge number $Z = A/2$ are injected at the reverse shock. This high injection efficiency results in the significant shock modification already at early stages of SNR expan-

sion while the thermal sub-shock compression ratio is close to 2.5 during the simulation. This is in agreement with the radio-observations of young extragalactic SNRs [23] and with the modeling of collisionless shocks [24]. Similar values of the injection efficiency were found in hybrid modeling (see e.g. [25]) and at the Earth bow shock in the solar wind [26].

As for the electron injection we assume a rather high injection energy of electrons $E_{inj} = 100$ MeV. This qualitatively corresponds to some models of suprathermal electron injection. Partially ionized ions accelerated at the shocks up to relativistic energies can produce multi-MeV electrons in the upstream region in the course of photo-ionization by Galactic optical and infrared radiation [27]. MeV electrons and positrons are also present in the radioactive supernova ejecta while gamma-rays from ^{56}Co decay in ejecta produce energetic electrons via Compton scattering in the circumstellar medium [28]. These energetic particles may be additionally pre-accelerated via stochastic acceleration in the turbulent upstream regions of the shocks.

Below we assume that electrons are injected at the forward shock with efficiency $\eta_-^f = 10^{-3} \dot{R}_f^2/c^2$ while positrons are injected at the reverse shock with efficiency $\eta_+^b = 10^{-6}$. These numbers are expected for the injection mechanisms mentioned above (see Sect.4 for details). Since electrons are considered as test particles our results can be easily rescaled for any other injection efficiency. The chosen injection rate at forward shock maintains the electron to proton ratio K_{-p} of the order of $K_{-p} \sim 10^{-3}$ throughout the simulation while time-independent positron injection at the reverse shock results in positron to ion ratio K_{+i} increase from $K_{+i} \sim 10^{-4}$ in the very beginning of SNR evolution up to $K_{+i} \sim 10^{-2}$ at several thousand years shortly before the disappearance of the reverse shock.

In the real SNR the ions are also injected at the forward shock. We do not consider this process here in order to find the spectra of ions produced by the reverse shock. Because of the same reason we assumed the absence of hydrogen in the ejecta. Although this is the case for Ia/b/c and IIb supernovae it
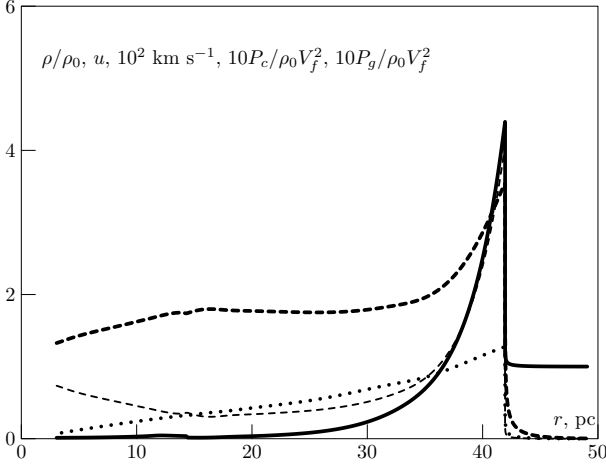
4

Figure 6: Radial dependencies of the gas density (thick solid line), the gas velocity (dotted line), CR pressure (thick dashed line) and the gas pressure (dashed line) at $t = 10^5$ yr. At this epoch the forward shock velocity is 164 km s^{-1}, its radius is 42 pc, magnetic field strength downstream of the forward shock is 23 μG.
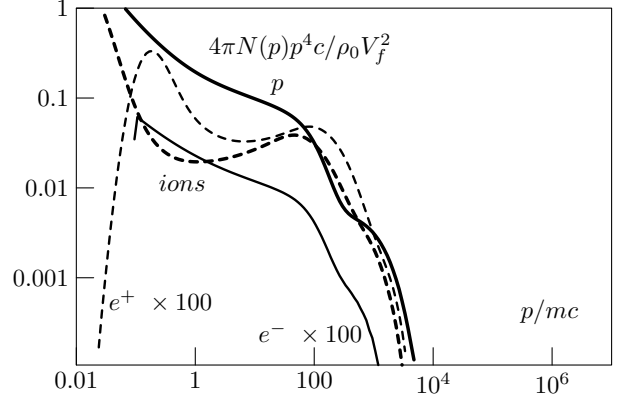

Figure 7: Spectra of accelerated particles at $t = 10^5$ yr. The spectrum of protons (thick solid line) and electrons (multiplied to the factor of 100, thin solid line) at the forward shock, ion spectrum (thick dashed line) and positron spectrum (multiplied to the factor of 100, thin dashed line) in the central part of the remnant are shown. Spectrum of ions is shown as the function of momentum per nucleon and normalized to baryonic number density.
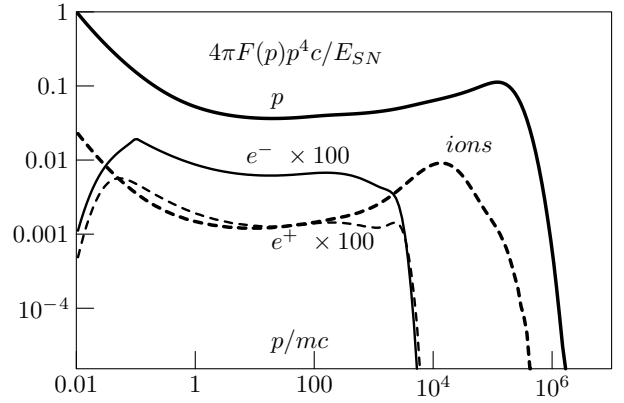

Figure 8: Spectra of particles produced in the supernova remnant during 10^5 yr. Spectrum of protons injected at the forward shock (thick solid line), spectrum of electrons injected at the forward shock (thin solid line), spectrum of ions injected at the reverse shock (thick dashed line) and the spectrum of positrons injected at the reverse shock (thin dashed line) are shown. Spectrum of ions is shown as the function of momentum per nucleon and normalized to the baryonic number density.

is not true for IIP supernovae. It is expected that the spectra of ions injected at the forward and reverse shock are similar to the spectra of protons. The production of CR ions at the forward shock was recently considered by Caprioli et al. [29].

The dependencies on time of the shock radii R_f and R_b, the forward and reverse shock velocities $V_f = \dot{R}_f$ and $V_b = \dot{R}_b$, CR energy E_{cr}/E_{SN} are shown in Fig.1. The calculations were performed until $t = 10^5$ yr, when the value of the forward shock velocity drops down to $\dot{R}_f = 164$ km s^{-1} and the forward shock radius is $R_f = 42$ pc.

At early times of SNR evolution the distance between reverse and forward shocks is only 10% of the remnant radius. This is less than 23% thickness for automodel Chevalier-Nadezhin solution with $k = 7$ [30] and should be attributed to a strong modification of both shocks by CR pressure. The reverse shock is strongly decelerated only when the forward shock sweeps the gas mass comparable with the ejecta mass at $t > 100$ yr and when the transition to the Sedov phase begins.

Radial dependencies of physical quantities at $t = 10^3$ yr are shown in Fig.2. The contact discontinuity between the ejecta and the interstellar gas is at $r = R_c = 5.6$ pc. The reverse shock in the ejecta is situated at $r = R_b = 5.1$ pc. At the Sedov stage the reverse shock moves in the negative direction and reach the center after seven thousand years after the supernova explosion. We stop the calculations in the region $r < R_b$ when the reverse shock radius $R_b < 0.1R_f$.

It should be noted that our one-dimensional calculations cannot adequately describe the development of the Rayleigh-Taylor instability of the contact discontinuity. In the real situation the supernova ejecta and the circumstellar gas are mixed by turbulent motions in this region (see e.g. MHD modeling of Jun & Norman [31]).

Spectra of accelerated protons and electrons at $t = 10^3$ yr are shown in Fig.3. At this epoch maximum energy of protons accelerated in this SNR is about 100 TeV, while higher energy

particles have already left the remnant.

Radial dependencies of physical quantities at later epoch $t = 10^4$ yr are shown in Fig.4. The reverse shock has reached the center of the remnant earlier. A weak reflected shock is clearly visible at $r = 5$ pc.

The spectra of particles ar $t = 10^4$ yr are shown in Fig.5.

Radial dependencies of physical quantities at the end of simulation at $t = 10^5$ yr are shown in Fig.6. At this epoch the remnant is deeply in Sedov stage. The contact discontinuity is at $r = 14$ pc.

The spectra of particles at $t = 10^5$ yr are shown in Fig.7. The shock modification is not strong because the Alfvénic Mach number is close to 6 and the corresponding Alfvén heating upstream of the forward shock results in the lower compression ratio and acceleration efficiency. That is why the spectra of particles are steeper in comparison with ones at earlier epochs.

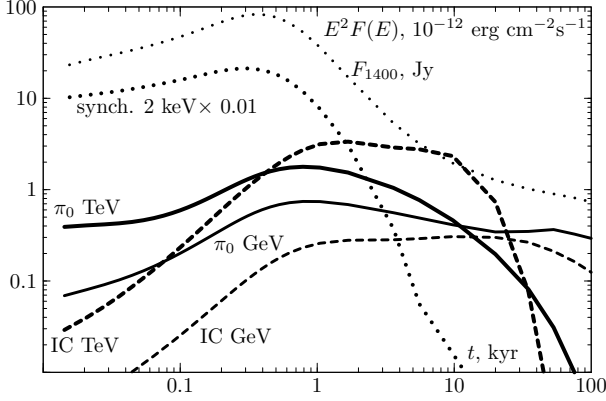The spectra of particles produced during the whole evolution

Figure 9: Dependencies on time of gamma-ray fluxes from SNR at distance 4 kpc. We show the gamma-ray flux at 1 TeV produced via pion decay (thick solid line) and via IC process (thick dashed line), gamma-ray flux at 1 GeV produced via pion decay (thin solid line) and via IC process (thin dashed line). For the sake of simplicity only IC scattering of microwave background photons was considered. The evolution of synchrotron X-ray flux at 2 keV (thick dotted line) and radio-flux at 1400 MHz F_{1400} (dotted line) are also shown.
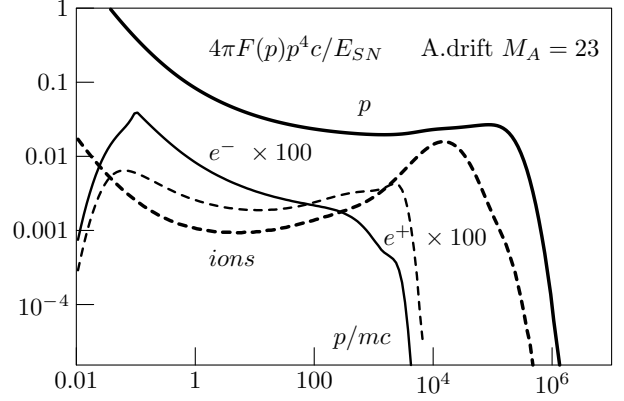

Figure 10: Spectra of particles produced in the supernova remnant during 10^5 yr in the model including the Alfvén drift downstream of the shocks. Spectrum of protons injected at forward shock (thick solid line), spectrum of electrons injected at the forward shock (thin solid line), spectrum of ions injected at the reverse shock (thick dashed line) and the spectrum of positrons injected at the reverse shock (thin dashed line) are shown. Spectrum of ions is shown as the function of momentum per nucleon and normalized to the baryonic number density.

of the remnant are shown in Fig.8. They are obtained as the sum of the spectra integrated throughout simulation domain and of the time-integrated diffusive flux at the simulation boundary at $r = 2R_f$. At $t = 10^5$ yr the maximum energy of currently accelerated particles drops down to 100 GeV because of nonlinear damping. Higher energy particles have already left the remnant. Note that stronger Kolmogorov-type damping with $g = 3$ will result even in lower energies of the order of 1 GeV. However we found that the spectra do not change in this case.

We found that the maximum energy of CR protons is somewhat less than 10^{15} eV. It is almost an order of magnitude lower in comparison with the results of Ptuskin et al. [10] where more optimistic assumptions $\eta_B = 1$ and the spatially-uniform CR diffusion coefficient upstream of the forward shock were used (cf. Eq.(7)).

Note that the synchrotron losses of run-away electrons and positrons were taken into account in our modeling. The cut-off energy of the leptonic spectra $\sim$ 5 TeV shown in Fig.8 is determined by the magnetic field strength $B_0 = 5\mu$G in the circumstellar medium and by the remnant age $t = 10^5$ yr.

Evolution of non-thermal emission produced in the SNR at distance 4 kpc is shown in Fig.9. It is worth noting that a significant part of the IC emission is produced in the central region of the remnant at late epochs when the reverse shock have disappeared. This is because the magnetic field is rather weak in these regions.

4. Discussion

Although only about 5% of supernova energy is transferred to the particles accelerated at the reverse shock, they cannot be neglected. First of all the ejecta has absolutely different composition in comparison with interstellar medium where the forward shock propagates. Since the solar abundance corresponds to 1% in the mass of heavy elements while the ejecta can contain up to 50% of heavy elements it is clear that the reverse shock will dominate in the production of heavy high-energy CR nuclei.

The relative input of the reverse shock at high energies is determined by the relative energetics of the reverse and forward shocks that is of the order of 1/10 for SNRs expanding in the uniform circumstellar medium.

According to our results, approximately 70% of supernova energy is transferred to particles accelerated by forward shock. It is significantly higher than the estimate of 10-20 % needed to maintain CR density in the Galaxy if the supernova rate is 1/30 yr. One of possibilities to resolve this contradiction is the assumption that CRs are accelerated only at small part of the forward shock surface. This can be due to the dependence of the proton and ion injection on the shock obliqueness [32]. This effect is observed in SN 1006 and in the interplanetary medium.

This effect does not influence strongly the ion injection at the reverse shock. It is expected that the random magnetic field is the main component of the field in the expanded ejecta. This is because the magnetic field of ejecta originates from the magnetic field of the exploded star. Thus the random magnetic field strength of the red super giant progenitor of IIP supernovae is of the order of 10^4 G similar to the magnetic field strength in the Sun interior while the regular field is of the order of 1 G. After a homogenous expansion from the initial stellar radius 10^{13} cm up to the radius 10^{19} cm of a young SNR the frozen-in magnetic field drops down to 10^{-8} G. Although this value is significantly lower than the magnetic field in the interstellar medium it is strong enough for acceleration of particles up to 100 GeV in SNRs. A more realistic non-homogenous expansion will result in the stretching of the field in the radial direction. This can increase the magnetic field strength and ion injection efficiency at the reverse shock. Magnetic fields can be also amplified by non-resonant CR streaming instability suggested by Bell [12]. If so the relative contribution of the reverse shock to the over-all CR spectrum increases.

The effect also depends on the type of the supernova explosion. It is known that acceleration at the reverse shock occurs in Cas A SNR [33, 34]. The progenitor of the core-collapse Cas A supernova had the radius of the order of $10^{12} - 10^{13}$ cm. On the other hand white dwarfs that are progenitors of Ia supernova explosions have small radii of the order of 10^9 cm. Interior magnetic field 10^8 G of the white dwarf will drop down to 10^{-12} G after the homogenous expansion of the young SNR. Such a weak magnetic field can result in the ineffective DSA at the reverse shock of Ia supernovae. This effect is probably observed in Tycho SNR (see Warren et al. [35] for details).

Another possibility to suppress the CR production is related with the Alfvén drift downstream of the forward shock [9]. It results in the steeper spectrum of CRs accelerated at the forward shock. On the other hand the Alfvén drift downstream of the reverse shock may produce even an opposite effect because the CR gradient is positive in this region (see Fig.2). As a result the input of the reverse shock will be significant at TeV energies.

The over-all spectrum according to this model is shown in Fig.10. The value of $\xi_A = -1$ instead of $\xi_A = 0$ is used downstream of the shocks. Because of the Alfvén drift the positron spectrum at reverse shock is significantly harder than the electron spectrum at the forward shock.

It should be noted that the spectra of ions accelerated at the reverse shock are harder than the proton spectra at the forward shock (see Figs 3,8) in spite of the same level of the shock modification for both shocks. This is because the shocks propagate in the media with different properties. When the reverse shock reach the flat part of the ejecta density distribution it propagates in the medium with decreasing in time density. That is why the number of freshly injected ions is low in comparison with higher energy particles accelerated earlier. It results in the spectral hardening. This effect is absent at the forward shock propagating in the medium with a constant density. The Alfvén drift strengthens this effect (see Fig.10).

We adjust the electron (positron) injection to produce a sufficient number of electrons and positrons. The spectra shown in Figs 8 and 10 can explain CR Galactic electrons and positrons. The expected positron injection efficiency from the radioactive decay of ^{44}Ti is estimated as $\eta_+^b \sim M_{Ti}/(44 M_{ej}) \sim 10^{-6}$ [28] for ^{44}Ti mass of the order of $\sim 10^{-4} M_\odot$ as observed in SNRs [36]. We used this number in our simulation. As for the electron injection at the forward shock the relative number of energetic electrons from photo-ionization of accelerated single charged He ions is of the order of $\eta_-^f \sim x_{He} \gamma^{-1} \ln^{-1}(p_{max}/mc) \dot{R}_f^2/c^2 \sim 10^{-3} \dot{R}_f^2/c^2$. Here $\gamma \sim I_{He}/\epsilon_{ph} \sim 10$ is the gamma-factor of single-charged He ion photo-ionized by galactic ultra-violet photons with energy $\epsilon_{ph} \sim 10$ eV and $I_{He} = 52$ eV is the ionization potential of helium. This slightly overestimates the electron injection in young SNRs where the acceleration is fast enough, γ is closer to $\gamma \sim 100$ and the ionization is provided by eV optical photons. However we used this crude estimate that is justified in old SNRs for electron injection in our simulations. This injection mechanism suggested by Morlino [27] produces one order of magnitude higher number of energetic electrons in comparison with the number $\eta_-^f \sim 10^{-7} R_{f,pc}^{-2}$ of Compton

scattered electrons energized by gamma-photons from ^{56}Co radioactive decay in supernova ejecta [28]. Here $R_{f,pc}$ is the forward shock radius expressed in parsecs.

The efficiency of electron (positron) acceleration at the reverse shock in SNRs can be observationally checked in the gamma-ray band. Young and middle-age ($t \sim 10^4$ yr) SNRs can be bright in TeV energies (see Fig.9). The electrons (positrons) accelerated before at the reverse shock do not strongly influenced by synchrotron losses in the weak magnetic field of the central part of the SNR and emit IC gamma-rays.

5. Conclusion

The main purpose of the present paper was the presentation of a new numerical code for the modeling of hydrodynamics and nonlinear shock acceleration in SNR. The code is described in details in five Appendixes. It develops the modeling of particle acceleration by spherical shocks fulfilled earlier by other authors [7, 8]. Besides some important technical details, the main novel features of our code include the particle acceleration by two shocks - forward and reverse, the evolving with a SNR age magnetic field, which determines the cosmic ray transport, the account for the Alfvén drift effects both upstream and downstream of the forward and reverse shocks. The first version of the model of acceleration [9] and a number of important applications including the explanation of the overall spectrum of galactic cosmic rays [10], and the modeling of particle acceleration and nonthermal radiation in SNR RX J1713.7-3946 [11] were developed upon our code refinements.

The special attention in the astrophysical applications of the modeling discussed in the present work was focused on the particle acceleration by the reverse SNR shock. It was shown that the reverse shock can give a non-negligible contribution to the production of CR ions and positrons as compared to the contribution of the forward shock. The spectra of particles accelerated at the reverse shock can be harder than the spectra at the forward shock, see Figures 8 and 10. It may offer a new interpretation of cosmic ray data [37] that suggests the presence of high energy primary positrons. The acceleration of positrons by the reverse shock moving through the ejecta material, which contains the positrons from ^{44}Ti radioactive decays, was proposed in [28]. It is also possible [38] that the hard spectrum of accelerated nuclei and the low abundance of hydrogen in the material of supernova ejecta accelerated by the reverse shock may explain the difference in the energy spectra of hydrogen and helium in cosmic rays. We plan detailed study of all these effects in a future work.

In the light of the problem of electron injection it is of interest that the models of suprathermal electron injection [28, 27] reproduce the required amount of Galactic CR electrons and positrons if the leptons are pre-accelerated up to $E_{inj} \sim 100$ MeV in the upstream regions of supernova shocks.

Appendix A. Details of the numerical method

We used the following change of variables upstream of the shocks:

$$\xi = \begin{cases} \frac{r}{R_b}, & r < R_b \\ \frac{r}{R_f}, & r > R_f. \end{cases} \tag{A.1}$$

and downstream of the shocks:

$$\eta = \begin{cases} \frac{r-R_c}{R_c-R_b}, & R_b < r < R_c, \\ \frac{r-R_c}{R_f-R_c}, & R_c < r < R_f. \end{cases} \tag{A.2}$$

We shall use the dimensionless parameters $\tilde{t} = \ln(R_f/R_0)$ instead of time t and $\zeta = \ln(p/mc)$ instead of momentum p. It is convenient to use the new variable $n(\zeta) = 4\pi c p^4 N(p)$ instead of momentum distribution $N(p)$. For the relativistic momenta $p \gg mc$ this variable corresponds to a partial energy density of cosmic rays.

In these new variables the equations (1)-(4) have the following form upstream of the shocks:

$$\frac{\partial}{\partial \tilde{t}} R_{f,b}^3 \xi^2 \rho = -\frac{\partial}{\partial \xi} R_{f,b}^2 \xi^2 (u - V_{f,b}\xi)\rho \frac{R_f}{V_f}, \tag{A.3}$$

$$\frac{\partial}{\partial \tilde{t}} R_{f,b}^3 \xi^2 \rho u = -\frac{\partial}{\partial \xi} R_{f,b}^2 \xi^2 (u - V_{f,b}\xi)\rho u \frac{R_f}{V_f} - R_{f,b}^2 \xi^2 \frac{R_f}{V_f}\frac{\partial}{\partial \xi}(P_c + P_g), \tag{A.4}$$

$$\frac{\partial}{\partial \tilde{t}} R_{f,b}^3 \xi^2 P_g = -\frac{\partial}{\partial \xi} R_{f,b}^2 \xi^2 (u - V_{f,b}\xi)P_g \frac{R_f}{V_f} - (\gamma_g - 1)R_{f,b}^2 \frac{R_f}{V_f}\left[(u - w)\xi^2 \frac{\partial}{\partial \xi}P_c + P_g \frac{\partial}{\partial \xi}\xi^2 u\right], \tag{A.5}$$

$$R_{f,b}^3 \xi^2 \frac{V_f}{R_f}\frac{\partial n}{\partial \tilde{t}} = \frac{\partial}{\partial \xi} R_{f,b}\xi^2 D \frac{\partial n}{\partial \xi} - R_{f,b}^2 \xi^2 (w - V_{f,b}\xi)\frac{\partial n}{\partial \xi} + \frac{R_{f,b}^2}{3}\left[\frac{\partial n}{\partial \zeta} - 4n\right]\frac{\partial}{\partial \xi}\xi^2 w, \tag{A.6}$$

Here indexes f and b are referred to the forward ($\xi > 1$) and reverse shock ($0 < \xi < 1$) respectively.
The equations (1)-(4) have the following form downstream of the shocks:

$$\frac{\partial}{\partial \tilde{t}} r^2 \Delta_{f,b}\rho = -\frac{\partial}{\partial \eta} r^2 u^{f,b}\rho \frac{R_f}{V_f}. \tag{A.7}$$

$$\frac{\partial}{\partial \tilde{t}} r^2 \Delta_{f,b}\rho u = -\frac{\partial}{\partial \eta} r^2 \frac{R_f}{V_f}(P_g + u^{f,b}\rho u) + r^2 \frac{R_f}{V_f}\left(\frac{2P_g \Delta_{f,b}}{r} - \frac{\partial}{\partial \eta}P_c\right), \tag{A.8}$$

$$\frac{\partial}{\partial \tilde{t}} r^2 \Delta_{f,b}e = -\frac{\partial}{\partial \eta} r^2 \frac{R_f}{V_f}(uP_g + u^{f,b}e) - wr^2 \frac{R_f}{V_f}\frac{\partial}{\partial \eta}P_c. \tag{A.9}$$

$$r^2 \Delta_{f,b}\frac{V_f}{R_f}\frac{\partial n}{\partial \tilde{t}} = \frac{\partial}{\partial \eta}\frac{r^2 D}{\Delta_{f,b}}\frac{\partial n}{\partial \eta} - r^2 w^{f,b}\frac{\partial n}{\partial \eta} + \frac{1}{3}\left[\frac{\partial n}{\partial \zeta} - 4n\right]\frac{\partial}{\partial \eta}r^2 w, \tag{A.10}$$

Here the speeds u^f and u^b are determined as $u^f = u - V_c(1-\eta) - \eta V_f$ and $u^b = u - V_c(1+\eta) + \eta V_b$ respectively. The corresponding CR advective speeds w^f and w^b are determined as $w^f = w - V_c(1-\eta) - \eta V_f$ and $w^b = w - V_c(1+\eta) + \eta V_b$ respectively. The quantities $\Delta_{f,b}$ are the distances between the forward shock and the contact discontinuity $\Delta_f = R_f - R_c$ and between the reverse shock and the the contact discontinuity $\Delta_b = R_c - R_b$. We introduced energy density of the gas $e = \frac{\rho u^2}{2} + \frac{P_g}{\gamma_g - 1}$. Then the equations (A7)-(A9) are written in the conservative form that is convenient for the numerical method. The radius r in the last equations should be expressed using Eq. (A2):

$$r = \begin{cases} R_c + \eta(R_f - R_c), & 0 < \eta < 1, \\ R_c + \eta(R_c - R_b), & -1 < \eta < 0. \end{cases} \tag{A.11}$$

8

Appendix B. Solution of hydrodynamic equations in the upstream regions

Since the flow upstream of the shocks is supersonic the hydrodynamic equations can be solved using the following implicit numerical scheme in these regions. Let introduce the grid ξ_i. Integration of equations (A3)-(A5) on ξ from ξ_i to ξ_{i+1} results in the following expressions for density ρ_i, velocity u_i and the gas pressure $P_{g,i}$ upstream of the forward shock ($\xi > 1$) at the grid knot with a number i in terms of ρ_{i+1} and u_{i+1}:

$$u_i G_i = \rho_i^{old} u_i^{old} \left(\frac{R_f^{old}}{R_f}\right)^3 - \rho_{i+1} u_{i+1} \frac{3\tau \xi_{i+1}^2 (u_{i+1} - V_f \xi_{i+1})}{V_f(\xi_{i+1}^3 - \xi_i^3)} - \frac{P_{c,i+1} + P_{g,i+1}^{old} - P_{c,i} - P_{g,i}^{old}}{V_f(\xi_{i+1} - \xi_i)}\tau \tag{B.1}$$

$$\rho_i = G_i \left[1 - \frac{3\tau \xi_i^2 (u_i - V_f \xi_i)}{V_f(\xi_{i+1}^3 - \xi_i^3)}\right]^{-1} \tag{B.2}$$

$$P_{g,i} = \left[P_{g,i}^{old}\left(\frac{R_f^{old}}{R_f}\right)^3 - P_{g,i+1}\frac{3\tau \xi_{i+1}^2 (u_{i+1} - V_f \xi_{i+1})}{V_f(\xi_{i+1}^3 - \xi_i^3)} - (\gamma_g - 1)(w_i - u_i)\tau \frac{P_{c,i+1} - P_{c,i}}{V_f(\xi_{i+1} - \xi_i)}\right] \times$$

$$\left[1 - 3\tau \frac{\xi_i^2(u_i - V_f\xi_i) + (\gamma_g - 1)(\xi_i^2 u_i - \xi_{i+1}^2 u_{i+1})}{V_f(\xi_{i+1}^3 - \xi_i^3)}\right]^{-1} \tag{B.3}$$

Here the superscript 'old' is referred to quantities at the previous time step and τ is the step in the dimensionless time $\tilde{t}$. The quantity G_i is given by the expression

$$G_i = \rho_i^{old}\left(\frac{R_f^{old}}{R_f}\right)^3 - \rho_{i+1}\frac{3\tau \xi_{i+1}^2 (u_{i+1} - V_f \xi_{i+1})}{V_f(\xi_{i+1}^3 - \xi_i^3)} \tag{B.4}$$

In spite of implicity Eqs (B1-B3) are readily solved recurrently from $i = i_{max}$ down to $i = f$ corresponding to the position of the forward shock. The value of the forward shock radius R_f is related with the forward shock radius R_f^{old} at the previous time step as $R_f = R_f^{old} \exp \tau$ in Eqs (B1-B4).

Performing the integration of equations (A3)-(A5) on ξ from ξ_{i-1} to ξ_i upstream of the reverse shock we obtain the expressions for for density, velocity ρ_i, u_i and and the gas pressure $P_{g,i}$ upstream of the reverse shock ($\xi < 1$) in terms of ρ_{i-1} and u_{i-1}:

$$u_i H_i' = u_i^{old} + u_{i-1}\frac{R_f \tau (u_i - V_b \xi_i)}{R_b V_f(\xi_i - \xi_{i-1})} - \frac{R_f(P_{c,i} + P_{g,i}^{old} - P_{c,i-1} - P_{g,i-1}^{old})}{R_b V_f(\xi_i - \xi_{i-1})}\tau \tag{B.5}$$

$$\rho_i = H_i\left[1 + \frac{3R_f \tau \xi_i^2 (u_i^{old} - V_b \xi_i)}{R_b V_f(\xi_i^3 - \xi_{i-1}^3)}\right]^{-1} \tag{B.6}$$

$$P_{g,i} = \left[P_{g,i}^{old}\left(\frac{R_b^{old}}{R_b}\right)^3 + P_{g,i-1}\frac{3R_f \tau \xi_{i-1}^2 (u_{i-1} - V_b \xi_{i-1})}{R_b V_f(\xi_i^3 - \xi_{i-1}^3)} - (\gamma_g - 1)(w_i - u_i)\tau \frac{R_f(P_{c,i} - P_{c,i-1})}{R_b V_f(\xi_i - \xi_{i-1})}\right] \times$$

$$\left[1 + 3R_f\tau\frac{\xi_i^2(u_i - V_b\xi_i) + (\gamma_g - 1)(\xi_i^2 u_i - \xi_{i-1}^2 u_{i-1})}{R_b V_f(\xi_i^3 - \xi_{i-1}^3)}\right]^{-1} \tag{B.7}$$

The quantities H_i and H_i' are given by expressions

$$H_i = \rho_i^{old}\left(\frac{R_b^{old}}{R_b}\right)^3 + \rho_{i-1}\frac{3R_f \tau \xi_{i-1}^2 (u_{i-1} - V_b \xi_{i-1})}{R_b V_f(\xi_i^3 - \xi_{i-1}^3)}, H_i' = 1 + \frac{R_f \tau (u_i^{old} - V_b \xi_i)}{R_b V_f(\xi_i - \xi_{i-1})} \tag{B.8}$$

Eqs (B5-B7) are solved recurrently from $i = 1$ to $i = b$ corresponding to the position of the reverse shock. The value of the new reverse shock radius R_b in Eqs (B5-B8) was extrapolated using the reverse shock radius R_b^{old} and velocity V_b^{old} as $R_b = R_b^{old} + V_b^{old} R_f \tau / V_f$.

9

Appendix C. Solution of hydrodynamic equations in the downstream regions

Hydrodynamical quantities are determined at the centers of the cells with the indexes $i+1/2$ in the downstream regions. We used an explicit numerical scheme of Trac & Pen [15] for solution of Eqs. (A7)-(A9). In accordance with these equations we use the following variables

$$U^1_{i+1/2} = \rho_{i+1/2}r^2_{i+1/2}\Delta_{f,b}, \ U^2_{i+1/2} = U^1_{i+1/2}u_{i+1/2}, \ U^3_{i+1/2} = r^2_{i+1/2}\Delta_{f,b}e_{i+1/2}, \tag{C.1}$$

and fluxes

$$F^1_{i+1/2} = \frac{R_f}{V_f}\rho_{i+1/2}r^2_{i+1/2}u^{f,b}_{i+1/2}, \ F^2_{i+1/2} = \frac{R_f}{V_f}r^2_{i+1/2}(\rho_{i+1/2}u_{i+1/2}u^{f,b}_{i+1/2} + P_{g,i+1/2}),$$

$$F^3_{i+1/2} = \frac{R_f}{V_f}r^2_{i+1/2}(e_{i+1/2}u^{f,b}_{i+1/2} + u_{i+1/2}P_{g,i+1/2}). \tag{C.2}$$

The variables $U^{\pm,l}_{i+1/2}$ are introduced as

$$U^{\pm,l}_{i+1/2} = c_s U^l_{i+1/2} \pm F^l_{i+1/2}, \ l = 1,2,3 \tag{C.3}$$

Here c_s is the so called freezing speed.

The values $U^{new,l}_{i+1/2}$ at the next instant of time are given by

$$U^{new,1}_{i+1/2} = U^1_{i+1/2} - \frac{\tau}{k_{f,b}}(F^1_{i+1} - F^1_i), \tag{C.4}$$

$$U^{new,2}_{i+1/2} = U^2_{i+1/2} - \frac{\tau}{k_{f,b}}(F^2_{i+1} - F^2_i) + \tau r_{i+1/2}\frac{R_f}{V_f}\left(2P_{g,i+1/2}\Delta_{f,b} - r_{i+1/2}\frac{P_{c,i+1} - P_{c,i}}{k_{f,b}}\right), \tag{C.5}$$

$$U^{new,3}_{i+1/2} = U^3_{i+1/2} - \frac{\tau}{k_{f,b}}(F^3_{i+1} - F^3_i) - \tau r^2_{i+1/2}w_{i+1/2}\frac{R_f}{V_f}\frac{P_{c,i+1} - P_{c,i}}{k_{f,b}}. \tag{C.6}$$

Here $k_{f,b}$ is the grid step downstream of the forward and reverse shock respectively. Note that a uniform grid in the downstream region was used.

The fluxes F^l_i at the grid knots between discontinuities are given by

$$F^l_i = 0.5(F^{+,l}_i + F^{-,l}_i), \ l = 1,2,3, \tag{C.7}$$

where the fluxes $F^{\pm,l}_i$ at the grid knots are given by

$$F^{+,l}_i = U^{+,l}_{i-1/2} + 0.5L(U^{+,l}_{i+1/2} - U^{+,l}_{i-1/2}, U^{+,l}_{i-1/2} - U^{+,l}_{i-3/2}), \ l = 1,2,3 \tag{C.8}$$

$$F^{-,l}_i = -U^{-,l}_{i+1/2} + 0.5L(U^{-,l}_{i+1/2} - U^{-,l}_{i-1/2}, U^{-,l}_{i+3/2} - U^{-,l}_{i+1/2}), \ l = 1,2,3. \tag{C.9}$$

Here the function $L(a,b)$ is the nonlinear flux limiter.

The numerical scheme is reduced to the first order Godunov's one for $L(a,b) = 0$ in Eqs. (C8), (C9). Such a scheme is very dissipative. The simplest second order scheme corresponds to $L(a,b) = a$. However it is unstable. One should use more complex flux limiters for stability. The different types of corresponding nonlinear limiters are available. Trac & Pen [15] used a so-called Van-Leer limiter:

$$L(a,b) = \begin{cases} \frac{2ab}{a+b}, \ ab > 0 \\ 0, \ ab \leqslant 0. \end{cases} \tag{C.10}$$

We used a more dissipative "minmod" limiter:

$$L(a,b) = \begin{cases} a, \ ab > 0, \ |a| < |b|, \\ b, \ ab > 0, \ |a| > |b|, \\ 0, \ ab \leqslant 0. \end{cases} \tag{C.11}$$

For calculations of fluxes $F^{\pm,l}_i$ near discontinuities we also use $L(a,b) = 0$ or $L(a,b) = a$.

The fluxes F_f^l and F_b^l just downstream of the forward and reverse shock at the knots with numbers $i = f$ and $i = b$ are calculated using hydrodynamical quantities just upstream of the forward and reverse shocks:

$$F_{f,b}^1 = \frac{R_f}{V_f}\rho_{f,b}R_{f,b}^2(u_{f,b} - V_{f,b}), \ \ F_{f,b}^2 = \frac{R_f}{V_f}R_{f,b}^2(\rho_{f,b}u_{f,b}(u_{f,b} - V_{f,b}) + P_{g,f,b}),$$

$$F_{f,b}^3 = \frac{R_f}{V_f}R_{f,b}^2(e_{f,b}(u_{f,b} - V_{f,b}) + u_{f,b}P_{g,f,b}). \tag{C.12}$$

The fluxes F_c^l at the position of the contact discontinuity at the knot with number $i = c$ are given by

$$F_c^1 = 0, \ \ F_c^2 = P'R_c^2 R_f/V_f, \ \ F_c^3 = V_c F_c^2,$$

where the pressure P' is found from the approximate solution of the Riemann problem for decay of an arbitrary discontinuity:

$$P' = \frac{P_{c+1/2}\sqrt{\rho_{c-1/2}} + P_{c-1/2}\sqrt{\rho_{c+1/2}} + (u_{c-1/2} - u_{c+1/2})\sqrt{\gamma_g P \rho_{c-1/2}\rho_{c+1/2}}}{\sqrt{\rho_{c-1/2}} + \sqrt{\rho_{c+1/2}}}. \tag{C.13}$$

Here $P = (P_{c-1/2} + P_{c+1/2})/2$.

Hydrodynamical quantities at the new time step are found using Eq. (C1) after the calculation of new positions of the discontinuities (see Appendix D).

For a stability of the numerical scheme considered the freezing speed c_s must be greater than the maximal sonic velocity. We use the following expression for c_s

$$c_s = \frac{R_f}{V_f}\max\left[\left(\sqrt{\gamma_g\frac{0.5(P_{c,i} + P_{c,i+1}) + P_{g,i+1/2}}{\rho_{i+1/2}}} + |u_{i+1/2}|\right)\Delta_{f,b}^{-1}\right], R_b < r_{i+1/2} < R_f \tag{C.14}$$

The time step τ was found from the relation $\tau = 0.5\max(k_f, k_b)/c_s$.

Appendix D. Calculation of the velocities of discontinuities

The velocities of discontinuities are found from the approximate solutions of the Riemann problem describing a decay of an arbitrary discontinuity. For the forward and reverse shocks the solution for the shock velocities V_f and V_b are the following:

$$V_f = u_f + \rho_f^{-1/2}\sqrt{\frac{\gamma_g + 1}{2}P_{f-1/2} + \frac{\gamma_g - 1}{2}P_f}. \tag{D.1}$$

$$V_b = u_b - \rho_b^{-1/2}\sqrt{\frac{\gamma_g + 1}{2}P_{b+1/2} + \frac{\gamma_g - 1}{2}P_b}. \tag{D.2}$$

The shock velocities are determined by upstream values $P_f, P_b, u_f, u_b, \rho_u, \rho_b$ and downstream values $P_{f-1/2}, P_{b+1/2}$ of the gas pressure, velocity and density.

The expression for the velocity of the contact discontinuity V_c is given by

$$V_c = \frac{u_{c-1/2}\sqrt{\rho_{c-1/2}} + u_{c+1/2}\sqrt{\rho_{c+1/2}} + \frac{P_{c-1/2}-P_{c+1/2}}{\sqrt{\gamma_g P}}}{\sqrt{\rho_{c-1/2}} + \sqrt{\rho_{c+1/2}}} \tag{D.3}$$

Here $P = (P_{c-1/2} + P_{c+1/2})/2$.

The new values for the radii $R_b, R_c, R_f = R_f^{old}\exp(\tau)$ and real time t are now found:

$$R_b = R_b^{old} + R_f^{old}\tau\frac{V_b + V_b^{old}}{V_f + V_f^{old}}\exp(0.5\tau), \tag{D.4}$$

$$R_c = R_c^{old} + R_f^{old}\tau\frac{V_c + V_c^{old}}{V_f + V_f^{old}}\exp(0.5\tau), \tag{D.5}$$

$$t = t^{old} + \frac{2R_f^{old}\tau}{V_f + V_f^{old}}\exp(0.5\tau). \tag{D.6}$$

Appendix E. Solution of CR transport equation

The finite difference scheme for Eqs (A6) and (A10) can be written in the following form:

$$a_i^j n_{i-1}^j + b_i^j n_i^j + c_i^j n_{i+1}^j = g_i^j \tag{E.1}$$

Here n_i^j are the values of n at the new time step calculated in the grid knot ξ_i or η_i and at ζ_j. We use the following coefficients upstream of the shocks

$$a_i^j = D_{i-1/2}^j R_{f,b} \frac{\xi_{i-1/2}^2}{\xi_i - \xi_{i-1}} + (w_i - V_{f,b}\xi_i)R_{f,b}^2\xi_i^2 \begin{cases} 0, \ \xi_i > 1, \\ 1, \ \xi_i < 1. \end{cases} , \tag{E.2}$$

$$c_i^j = D_{i+1/2}^j R_{f,b} \frac{\xi_{i+1/2}^2}{\xi_{i+1} - \xi_i} - (w_i - V_{f,b}\xi_i)R_{f,b}^2\xi_i^2 \begin{cases} 1, \ \xi_i > 1, \\ 0, \ \xi_i < 1. \end{cases} , \tag{E.3}$$

$$b_i^j = -a_i^j - c_i^j - \frac{V_f R_{f,b}^3}{3R_f\tau}(\xi_{i+1/2}^3 - \xi_{i-1/2}^3) - \frac{d_i R_{f,b}^2}{3} \begin{cases} 4 - h^{-1}, \ d_i \leqslant 0, \\ 4, \ d_i > 0. \end{cases} , \ d_i = \xi_{i+1/2}^2 w_{i+1/2} - \xi_{i-1/2}^2 w_{i-1/2}, \tag{E.4}$$

$$g_i^j = -\frac{V_f R_{f,b}^3}{3R_f\tau}(\xi_{i+1/2}^3 - \xi_{i-1/2}^3)n_i^{j,old} - \frac{d_i R_{f,b}^2}{3h} \begin{cases} -n_i^{j-1}, \ d_i \leqslant 0, \\ n_i^{j+1,old} - n_i^{j,old}, \ d_i > 0. \end{cases} . \tag{E.5}$$

The corresponding coefficients downstream of the shocks are given by

$$a_i^j = D_{i-1/2}^j \frac{r_{i-1/2}^2}{\Delta_{f,b}(\eta_i - \eta_{i-1})} + w_i^{f,b}r_i^2 \begin{cases} 0, \ \eta_i > 0, \\ 1, \ \eta_i < 0. \end{cases} , \tag{E.6}$$

$$c_i^j = D_{i+1/2}^j \frac{r_{i+1/2}^2}{\Delta_{f,b}(\eta_{i+1} - \eta_i)} - w_i^{f,b}r_i^2 \begin{cases} 1, \ \eta_i > 0, \\ 0, \ \eta_i < 0. \end{cases} , \tag{E.7}$$

$$b_i^j = -a_i^j - c_i^j - \frac{V_f}{3R_f\tau}(r_{i+1/2}^3 - r_{i-1/2}^3) - \frac{d_i}{3} \begin{cases} 4 - h^{-1}, \ d_i \leqslant 0, \\ 4, \ d_i > 0. \end{cases} , \ d_i = r_{i+1/2}^2 w_{i+1/2} - r_{i-1/2}^2 w_{i-1/2}, \tag{E.8}$$

$$g_i^j = -\frac{V_f}{3R_f\tau}(r_{i+1/2}^3 - r_{i-1/2}^3)n_i^{j,old} - \frac{d_i}{3h} \begin{cases} -n_i^{j-1}, \ d_i \leqslant 0, \\ n_i^{j+1,old} - n_i^{j,old}, \ d_i > 0. \end{cases} . \tag{E.9}$$

The forward and reverse shocks are situated at knots with numbers $i = f$ and $i = b$ respectively. The coefficients at these knots are given by

$$a_f^j = D_{f-1/2}^j \frac{r_{f-1/2}^2}{\Delta_f(\eta_f - \eta_{f-1})}, \ c_f^j = D_{f+1/2}^j R_f \frac{\xi_{f+1/2}^2}{\xi_{f+1} - \xi_f}, \tag{E.10}$$

$$b_f^j = -a_f^j - c_f^j - \frac{V_f}{3R_f\tau}(R_f^3\xi_{f+1/2}^3 - r_{f-1/2}^3) - \frac{4 - h^{-1}}{3}d_f, \ d_f = R_f^2\xi_{f+1/2}^2 w_{f+1/2} - r_{f-1/2}^2 w_{f-1/2}, \tag{E.11}$$

$$g_f^j = -\frac{V_f}{3R_f\tau}(R_f^3\xi_{f+1/2}^3 - r_{f-1/2}^3)n_f^{j,old} - \eta^f(V_f - w_f)\rho_f \frac{p_{inj}^f c}{mh}\delta(j, j_f) + \frac{d_f}{3h}n_f^{j-1}, \tag{E.12}$$

and

$$a_b^j = D_{b-1/2}^j R_b \frac{\xi_{b-1/2}^2}{\xi_b - \xi_{b-1}}, c_b^j = D_{b+1/2}^j \frac{r_{b+1/2}^2}{\Delta_b(\eta_{b+1} - \eta_b)}, \tag{E.13}$$

$$b_b^j = -a_b^j - c_b^j - \frac{V_f}{3R_f\tau}(r_{b+1/2}^3 - R_b^3\xi_{b-1/2}^3) - \frac{4 - h^{-1}}{3}d_b, \ d_b = r_{b+1/2}^2 w_{b+1/2} - R_b^2\xi_{b-1/2}^2 w_{b-1/2}, \tag{E.14}$$

$$g_b^j = -\frac{V_f}{3R_f\tau}(r_{b+1/2}^3 - R_b^3\xi_{b-1/2}^3)n_b^{j,old} - \eta^b(w_b - V_b)\rho_b \frac{p_{inj}^b c}{mh}\delta(j, j_b) + \frac{d_b}{3h}n_b^{j-1}. \tag{E.15}$$

12

Here $\delta(j, l)$ is the Kronecker's symbol while j_f and j_b are numbers of the momentum grid knots corresponding to injection momenta p_f and p_b respectively.

The contact discontinuity is situated at the knot $i = c$. The coefficients at this knot are given by

$$a_c^j = D_{c-1/2}^j \frac{r_{c-1/2}^2}{\Delta_b(\eta_c - \eta_{c-1})}, \ c_c^j = D_{c+1/2}^j \frac{r_{c+1/2}^2}{\Delta_f(\eta_{c+1} - \eta_c)}, \tag{E.16}$$

$$b_c^j = -a_c^j - c_c^j - \frac{V_f}{3R_f\tau}(r_{c+1/2}^3 - r_{c-1/2}^3) - \frac{d_c}{3}\begin{cases} 4 - h^{-1}, \ d_c \leqslant 0 \\ 4, \ d_c > 0 \end{cases}, \ d_c = r_{c+1/2}^2 w_{c+1/2} - r_{c-1/2}^2 w_{c-1/2}, \tag{E.17}$$

$$g_c^j = -\frac{V_f}{3R_f\tau}(r_{c+1/2}^3 - r_{i-1/2}^3)n_c^{j,old} - \frac{d_c}{3h}\begin{cases} -n_c^{j-1}, \ d_c \leqslant 0 \\ n_c^{j+1,old} - n_c^{j,old}, \ d_c > 0 \end{cases}. \tag{E.18}$$

We use a standard method to solve the tridiagonal set of equations (E1) (e.g. Godunov [39]). At first the following coefficients $L_{i+1/2}^j$ and $K_{i+1/2}^j$ are recurrently calculated from $i = 1$ up to $i = i_{max} - 1$:

$$L_{i+1/2}^j = -\frac{c_i^j}{a_i^j L_{i-1/2}^j + b_i^j}, \ K_{i+1/2}^j = \frac{g_i^j - a_i^j K_{i-1/2}^j}{a_i^j L_{i-1/2}^j + b_i^j}. \tag{E.19}$$

The values $L_{1/2}^j = 1$ and $K_{1/2}^j = 0$ correspond to the boundary condition $n_0^j = n_1^j$ at the center of the remnant. The functions n_i^j are calculated recurrently from $i = i_{max} - 1$ down to $i = 0$ as

$$n_i^j = L_{i+1/2}^j n_{i+1}^j + K_{i+1/2}^j. \tag{E.20}$$

We put $n_i^j = 0$ at $i = i_{max}$. This describes an absorbtion of particles at the boundary of the simulation domain. The equations (E19), (E20) are recurrently used for all values of j starting with the lowest energies at $j = j_{min} + 1$.

Appendix F. Initial conditions and the code performance

We use a uniform spacial grid downstream of the shocks and the following non-uniform grids upstream of the forward shock

$$\xi_i = 1 - \xi_{min} + \xi_{min} \exp[(i - f)k_1], \ k_1 = \ln[(\xi_{max} + \xi_{min} - 1)/\xi_{min}]/(i_{max} - f) \tag{F.1}$$

and upstream of the reverse shock

$$\xi_i = 2ik_4 + \left[\ln\left(1 + (2\xi_{min})^{(1-2ik_4)}\right) - \ln(1 + 2\xi_{min})\right]/\ln(2\xi_{min}), \ k_4 = 1/b. \tag{F.2}$$

Here the parameter ξ_{max} describes the ratio of radii of the simulation domain and forward shock. This parameter is constant during the simulation. We use the value $\xi_{max} = 2$. The value of the parameter $\xi_{min} \sim 10^{-11}$ should be small enough to resolve the spacial variation scale of the lowest energy cosmic rays upstream of the shocks.

We use the following profiles of the gas density, velocity and pressure at the initial moment of time $\tilde{t} = 0$:

$$\begin{cases} \rho = \rho_0, \ u = 0, \ P_g = P_0, \ r > R_f, \\ \rho = 4\rho_0, \ u = 0.75V_f, \ P_g = 0.75\rho_0 V_f^2, \ R_b < r < R_f, \\ \rho = \rho_0(r/R_b)^{-k}, \ u = 1.5V_f r/R_b, \ P_g = 0, \ r_{ej} < r < R_b, \\ \rho = \rho_0(r_{ej}/R_b)^{-k}, \ u = 1.5V_f r/R_b, P_g = 0, \ r < r_{ej}. \end{cases} \tag{F.3}$$

Here ρ_0 and P_0 are the gas density and pressure in the circumstellar medium while $r_{ej} = 2V_{ej}R_b/3V_f$ is the initial radius of the flat part of the ejecta density distribution. The initial velocities of the reverse shock and contact discontinuity are $V_b = 0.5V_f$ and $V_c = 0.75V_f$ respectively. Their initial radii can be chosen rather arbitrary. We use values $R_b = 0.9R_f$ and $R_c = 0.95R_f$.

The initial cosmic ray number density is zero. At every time step the system of equations (1)-(4) is solved in the following order:

1) The hydrodynamical equations are solved in the upstream regions (see Appendix B).

2) These equations are solved in the downstream regions and the speeds of discontinuities are determined (see Appendix C and D).

3) The parameters of CR transport depending on the hydrodynamical quantities are calculated.

4) CR transport equation is solved (see appendix E). Cosmic ray pressure is calculated.

It is important to note that we use the finite difference method for solution of CR transport equations even at the shock positions at grid knots $i = f$ and $i = b$ (see Eqs. (E10-E15)). These equations contain terms originating from the first derivative on time (see

terms containing τ in Eqs.(E10-E15)). These terms will not appear if we use exact boundary conditions at the shock fronts which can be derived by integration of Eq. (4) in the vicinity of the shocks. Our method permits to use relatively large time steps τ while the use of the exact boundary conditions results in a numerical instability for the large time steps. Physically this is because the low energy particles have very small acceleration times in the case of Bohm-like diffusion. This results in the numerical instabilities. It is possible to use many iterations at every time step [7] or to use very small time steps near the shock front [8] to avoid this problem. This results in significantly longer times of simulations.

The numerical scheme with Eqs. (E10-E15) artificially increases acceleration time of low-energy particles and makes the calculations to be stable. This means that our method can not be used for simulations of fast varying processes. However if the shocks propagate in the smooth environment then the low-energy particles are accelerated in a quasi-steady regime and our method is well justified.

The numerical results shown in Figs (1)-(10) were obtained using the grid with 200×200 radius-momentum cells in the every of four regions (two upstream and two downstream regions of the shocks). The initial radius of the flat part of the ejecta density distribution r_{ej} is $r_{ej} = R_b/6$. The calculation of the remnant evolution takes two hours at PC. The total energy is conserved with 5% accuracy. Preliminary results can be obtained using ten times faster crude calculations with 100×100 grid.

References

[1] Krymsky, G.F. 1977, Soviet Physics-Doklady, 22, 327
[2] Bell, A.R., 1978, MNRAS, 182, 147
[3] Axford, W.I., Leer, E., Skadron, G., 1977, Proc. 15th Int. Cosmic Ray Conf., Plovdiv, 90, 937
[4] Blandford, R.D., & Ostriker, J.P. 1978, ApJ, 221, L29
[5] Malkov, M.A., & Drury, L.O'C, 2001, Reports on Progress in Physics, 64, 429
[6] Aharonian, F.A., Buckley, J., Kifune, T., & Sinnis, G. 2008, Rep. Prog. Phys., 71, 096901
[7] Berezhko, E.G., Elshin, V.K., Ksenofontov, L.T., 1994, Astropart. Phys. 2, 215
[8] Kang, H., Jones, T.W., 2006, Astropart. Phys. 25, 246
[9] Zirakashvili, V.N., Ptuskin, V.S., 2008 Proc. of Intern. Gamma-Ray Symposium, Heidelberg, Germany, 7-11 July 2008, 336
[10] Ptuskin, V.S., Zirakashvili, V.N., & Seo, E.S., 2010, ApJ 718, 31
[11] Zirakashvili, V.N., Aharonian, F.A., 2010, ApJ, 708, 965
[12] Bell, A.R., 2004, MNRAS, 353, 550
[13] Zirakashvili, V.N., Ptuskin, V.S., 2008, ApJ 678, 939
[14] Lagage, P.O., & Cesarsky, C.J., 1983, A&A, 118, 223
[15] Trac, H., Pen, U. 2003, Publ. Astron. Soc. Pacific 115, 303
[16] Völk, H.J., Berezhko, E.G., & Ksenofontov, L.T., 2005, A&A, 433, 229
[17] McKenzie, J.F., & Völk, H.J., 1982, A&A, 116, 191
[18] Caprioli, D., Blasi, P., Amato, E., & Vietri, M., 2008, ApJ. 679, L139
[19] Ptuskin, V.S., & Zirakashvili, V.N. 2005, A&A, 429, 755
[20] Vladimirov, A., Ellison, D.C., & Bykov, A., 2006, ApJ, 652, 1246
[21] Amato, E., & Blasi, P., 2006, MNRAS, 371, 1251
[22] Chevalier, R., 1982, ApJ, 259, 302
[23] Chevalier, R. & Fransson, C., 2006, ApJ 651, 381
[24] Zirakashvili, V.N. 2007, A&A 466, 1
[25] Giacalone, J., Burgess, D., Schwartz, S.J., Ellison, D. C., & Benett.L. 1997, JGR 102, 19789
[26] Ellison, D. C., Möbius, E., & Paschmann, G., 1990, ApJ 352, 376
[27] Morlino, G., 2011, MNRAS 412, 2333
[28] Zirakashvili, V.N., Aharonian, F.A., 2010, arXive:1011.4775
[29] Caprioli, D., Blasi, P., & Amato, E., 2011, Astropart. Phys. 34, 447
[30] Chevalier, R., 1982, ApJ, 258, 790
[31] Jun, B., & Norman, M.L., 1996, ApJ 465, 800
[32] Berezhko, E.G., & Völk, H.J. 2004a, A&A 419, L27
[33] Helder, E.A., & Vink, J., 2008, ApJ 686, 1094
[34] Uchiyama, Y., & Aharonian, F., 2008, ApJ 677, L105
[35] Waren, J.S., et al., 2005, ApJ 634, 376
[36] M.Renaud *et al.*, 2006, Astrophys. J. 647, L41
[37] Adriani, O. et al., 2009, Nature 458, 607
[38] Ptuskin, V.S., Zirakashvili, V.N., & Seo, E.S., 2011, Proc. 32nd ICRC, Beijin
[39] Godunov, S.K., 1971, Equations of mathematical physics, Moscow (in Russian)